Polarity-dependent twist-controlled resonant tunneling device based on few-layer WSe₂

Kei Kinoshita [1], Rai Moriya [1,*], Shota Okazaki,[2] Yijin Zhang [1], Satoru Masubuchi,[1]
Kenji Watanabe [3], Takashi Taniguchi [4], Takao Sasagawa [2], and Tomoki Machida [1,†]

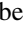[1]*Institute of Industrial Science, University of Tokyo, 4-6-1 Komaba, Meguro, Tokyo 153-8505, Japan*

[2]*Laboratory for Materials and Structures, Tokyo Institute of Technology, 4259 Nagatsuta, Yokohama, Kanagawa 226-8503, Japan*

[3]*Research Center for Electronic and Optical Materials, National Institute for Materials Science, 1-1 Namiki, Tsukuba 305-0044, Japan*

[4]*International Center for Materials Nanoarchitectonics, National Institute for Materials Science, 1-1 Namiki, Tsukuba 305-0044, Japan*

Few-layer (FL) transition metal dichalcogenides have been found to exhibit discrete subbands, called van der Waals quantum well (vdWQW) states, resulting from out-of-plane quantum confinement. In this study, we reveal the twisted-resonant tunneling characteristics of a vdWQW device using a three-layer (3L) WSe₂/*h*-BN/3L-WSe₂ junction with different twist angles θ_{tunnel} between the two 3L WSe₂ flakes. Using an ambipolar graphene contact to WSe₂, two primary vdWQW states of 3L WSe₂ located in the conduction band (CB) and valence band (VB) were investigated. We found that while the current peak positions due to the electron resonant tunneling between the CB-QW states significantly change with θ_{tunnel} having a periodicity of 60°, the hole resonant tunneling between the VB-QW states exhibits no θ_{tunnel} dependence; these are due to different angular dispersions of two vdWQWs. The results highlight the different twistronic properties of CB and VB vdWQWs in FL WSe₂.

I. INTRODUCTION

When transition metal dichalcogenides (TMDs) become few layer (FL) in thickness, quantized subbands are formed in the band owing to the quantization of the electronic states in the out-of-plane direction. Because the atomically flat van der Waals (vdW) surfaces of FL TMDs allow the realization of such quantum confinement, these quantized subbands can be regarded as a naturally formed quantum well (QW) structure, namely, the van der Waals QW (vdWQW) [1–3]. Such vdWQW is a unique property of FL TMDs and is absent for monolayer-thick TMDs [1,2]. It has been reported that the energy level spacings between these vdWQW states can be tuned by selecting different materials and thicknesses, allowing a broad range of technologically important wavelengths, from the near infrared to the far infrared, to be covered [1,4,5]. In addition, we recently demonstrated resonant tunneling in a FL-WSe₂/*h*-BN/FL-WSe₂ vdW double QW structure with superior peak-to-valley ratios (PVRs) compared to those in other layered-material-based resonant tunneling devices [6]. Because of these technological advantages, studies on vdWQW states in other layered materials such as InSe and black phosphorus were also reported recently [7–9]. These make vdWQW devices attractive for electronic and optoelectronic applications.

Despite these technological interests, a detailed understanding of the vdWQW remains lacking. For example, all previous experimental studies of vdWQW states in FL TMD have focused on those states in the valence band (VB) Γ point [2,3,6], and no serious attempts have been made to examine other vdWQW states. Here, we note that vdWQW states in the FL TMD are present in both the conduction band (CB) and VB, and their properties are quite different, as discussed below. The band structure of three-layer (3L) WSe₂ calculated using density functional theory (DFT) is shown in Fig. 1(a). The calculation reveals the presence of quantized subbands in both the CB and VB owing to the formation of vdWQW states, as expressed by the orange and green rectangular outlines. The bottom of the CB subbands is located at the Q point between the Γ and K points, and this point is the energy minimum of the CB. At this point, the number of subbands changes with the number of WSe₂ layers, N, and is equal to N for even N and $N + 1$ for odd N (subband energy calculations for monolayer to six-layer WSe₂ are given in Appendix A). This difference is due to the presence of inversion symmetry (asymmetry) in the even- (odd-) layer WSe₂. Because the even-layer WSe₂ possesses an inversion symmetry, all the subbands are spin degenerate; thus the number of subbands is equal to the layer number N. In contrast, inversion asymmetry in the odd-layer WSe₂ lifts spin degeneracy for one of the subbands at the Q point, resulting in the number of subbands at this point being equal to $N + 1$. Thus 3L WSe₂ has four subbands at the Q point of the CB, as shown in Fig. 1(a). Here, the second and third subbands at the Q point are spin polarized owing to spin-orbit interactions, whereas the first and fourth subbands are
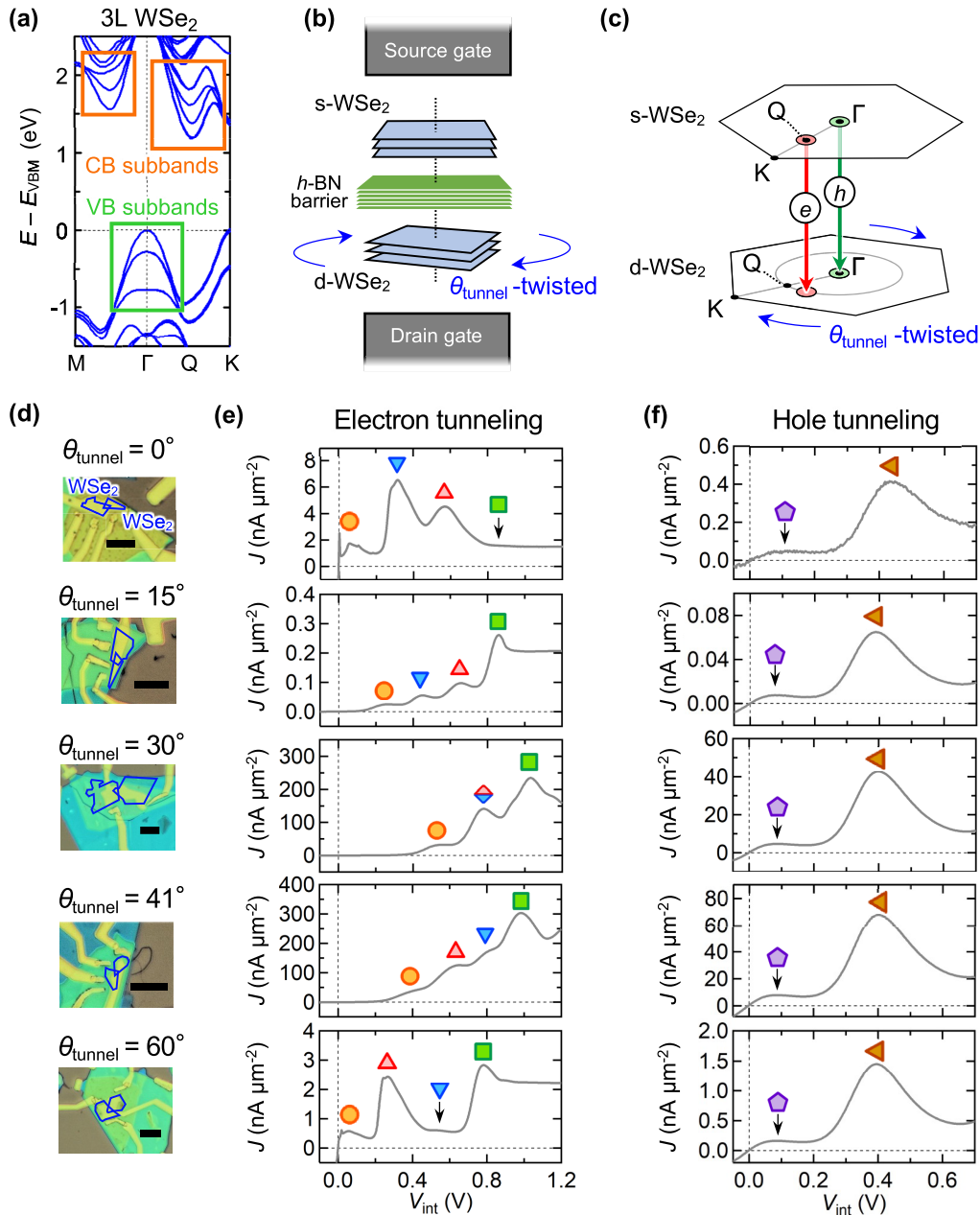
*moriyar@iis.u-tokyo.ac.jp
†tmachida@iis.u-tokyo.ac.jp

FIG. 1. (a) Band structure of three-layer (3L) WSe$_2$. Quantized subbands, highlighted by the orange and green rectangular outlines, are formed in both the conduction band (CB) and valence band (VB). The valence band maximum (VBM) energy is set to 0 eV. The energies were obtained using density functional theory (DFT) calculations. (b) Schematic of measured tunnel junction of 3L-WSe$_2$/few-layer (FL) h-BN/3L-WSe$_2$ van der Waals (vdW) heterostructure. The angular difference between the in-plane crystal orientations of the source WSe$_2$ (s-WSe$_2$) and drain WSe$_2$ (d-WSe$_2$) is controlled by the twist angle θ_{tunnel}. (c) Schematic of the first Brillouin zone (BZ) of s-WSe$_2$ and d-WSe$_2$ and momentum-conserved resonant tunneling. The BZ of d-WSe$_2$ is rotated by θ_{tunnel} around the Γ point with respect to that of s-WSe$_2$. Electrons and holes tunnel from the Q and Γ points, respectively. (d) Optical micrographs of the fabricated devices with $\theta_{tunnel} = 0°$, 15°, 30°, 41°, and 60° (scale bars, 10 μm; junction areas, 1.9 μm^2 for 0°, 3.2 μm^2 for 15°, 6.5 μm^2 for 30°, 0.4 μm^2 for 41°, and 5.2 μm^2 for 60°). (e) J-V_{int} characteristics for electron tunneling from each device in (d), measured at 2 K. Gate-voltage conditions: $V_{sg} = 15$ V, $V_{dg} = 100$ V for 0°; $V_{sg} = 10$ V, $V_{dg} = 85$ V for 15°; $V_{sg} = 100$ V, $V_{dg} = 17$ V for 30°; $V_{sg} = 70$ V, $V_{dg} = 10$ V for 41°; and $V_{sg} = 15$ V, $V_{dg} = 85$ V for 60°. (f) J-V_{int} characteristics for hole tunneling from each device in (d), measured at 300 K. Gate voltage conditions: $V_{sg} = -10.5$ V, $V_{dg} = -75$ V for 0°; $V_{sg} = -6$ V, $V_{dg} = -70$ V for 15°; $V_{sg} = -100$ V, $V_{dg} = -12$ V for 30°; $V_{sg} = -7$ V, $V_{dg} = -90$ V for 41°; and $V_{sg} = -13$ V, $V_{dg} = -85$ V for 60°.

spin degenerate [1,2]. In contrast, the top of the VB subbands is located at the Γ point, and the number of subbands at this point is equal to the number of layers N; they are all spin degenerate [1,2]. Therefore, the band structure calculations

show that the vdWQW states in the CB and VB of FL WSe$_2$ exhibit different momentum and spin states. However, no experimental attempts have been made to uncover the nature of these states. In this study, we utilized twist-controlled resonant
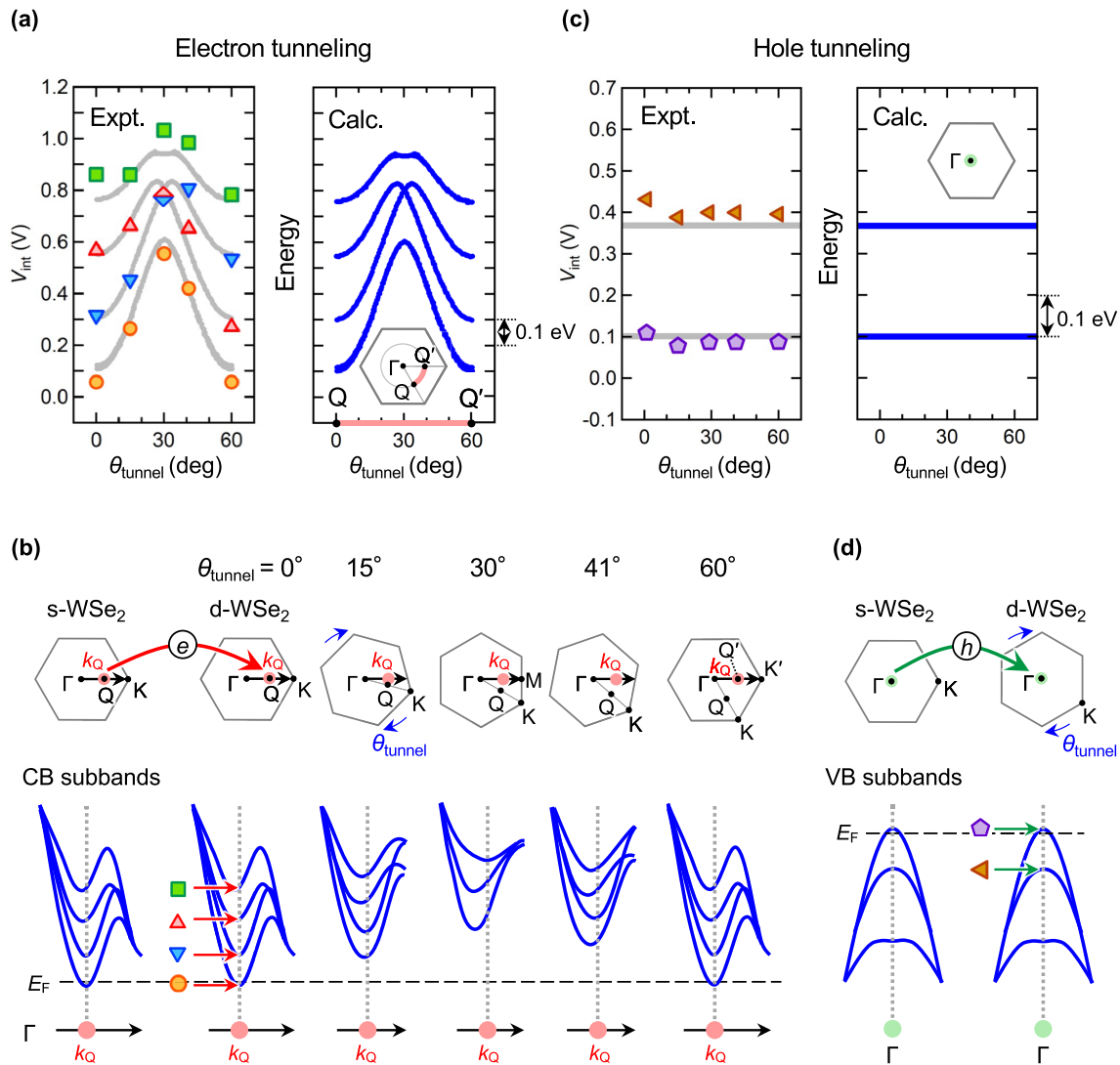
FIG. 2. [(a), (c)] (Left) Plot of V_{int} for each peak in the J-V_{int} curves of (a) electron tunneling [shown in Fig. 1(e)] and (c) hole tunneling [shown in Fig. 1(f)] versus θ_{tunnel}. (Right) DFT-calculated subband energies (a) along the Q-Q' angular direction in the CB and (c) at the Γ point in the VB. The calculation results are plotted as gray traces on the left panel. (b) (Upper part) Illustration of the BZ of s-WSe$_2$ and d-WSe$_2$ under $\theta_{tunnel} = 0°$, $15°$, $30°$, $41°$, and $60°$. The electron tunnels between s-WSe$_2$ and d-WSe$_2$ with momentum k_Q conserved. Lower part: Subband structure of s-WSe$_2$ along the Γ-Q-K direction and that of d-WSe$_2$ along the aligned direction with s-WSe$_2$ for each θ_{tunnel}. The vertical dotted lines indicate the constant momentum k_Q. (d) Upper part: Illustration for the BZ of s-WSe$_2$ and d-WSe$_2$. Hole tunnels between the Γ points of s-WSe$_2$ and d-WSe$_2$ with momentum conserved for any θ_{tunnel}. Lower part: Subband structures of s-WSe$_2$ and d-WSe$_2$ around the Γ point.

tunneling, which is highly sensitive to the band dispersion of electrode materials [10–12], to investigate the vdWQW states in the CB and VB of 3L WSe$_2$.

II. RESULTS

A schematic of the fabricated vdW double QW device is shown in Fig. 1(b) (see Appendix B, for details of the device fabrication). The tunneling current flowing through the 3L-WSe$_2$/FL-h-BN/3L-WSe$_2$ vdW tunnel junction was measured. The device has a dual-gated structure to independently control the carrier density of the two 3L WSe$_2$ flakes. As the WSe$_2$ flakes used in this experiment exhibit nearly intrinsic characteristics, the Fermi levels of WSe$_2$ are located

within the band gap without the application of gate voltages. When positive source and drain gate voltages (V_{sg} and V_{dg}) are applied, electrons accumulate at the bottom of the CB, located at the Q point of source WSe$_2$ (s-WSe$_2$) and drain WSe$_2$ (d-WSe$_2$) [see Fig. 1(a)]. Under these conditions, the interlayer bias V_{int} between s-WSe$_2$ and d-WSe$_2$ induces electron tunneling from the s-WSe$_2$ Q point into d-WSe$_2$ through the h-BN tunneling barrier. Similarly, when negative gate voltages of V_{sg} and V_{dg} are applied, holes accumulate at the top of the VB, located at the Γ point of the s- and d-WSe$_2$ layers. In this state, the application of V_{int} induces hole tunneling from the s-WSe$_2$ Γ point into d-WSe$_2$. In the device, we used a graphene vdW contact to the 3L WSe$_2$ because this contact demonstrates both n- and p-type carrier injection
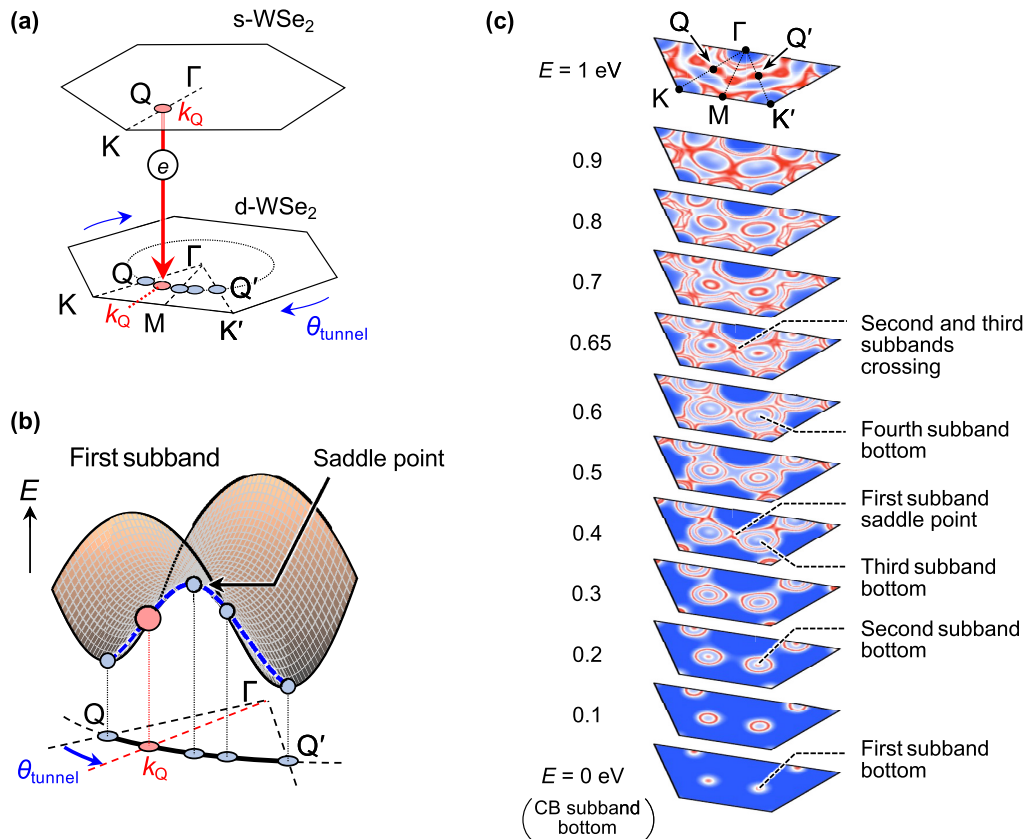
FIG. 3. [(a), (b)] Schematics of (a) momentum-conserved electron resonant tunneling between s-WSe$_2$ and d-WSe$_2$ and (b) tracking the band energy of the CB first subband along the Q-Q' angular direction. At different θ_{tunnel} values, electrons tunnel from the s-WSe$_2$ Q valley to d-WSe$_2$ at corresponding angular positions along the Q-Q' valley with their momentum k_Q conserved. (c) Calculated constant-energy plots for the CB subbands of 3L WSe$_2$ from $E = 0$ eV (subband bottom) to 1 eV.

into WSe$_2$ (see Appendix C, for the electrical properties of the graphene/WSe$_2$ heterojunction). The tunnel junction was fabricated using the vdW pickup method, starting with laser precutting of a 3L WSe$_2$ flake [13,14]. Junctions with specific relative in-plane crystal orientations of the s-WSe$_2$ flake and the d-WSe$_2$ flake were fabricated. Here, the angular difference between the in-plane crystal orientations of s-WSe$_2$ and d-WSe$_2$ in the tunnel junction is referred to as the twist angle, θ_{tunnel}. For example, when s-WSe$_2$ and d-WSe$_2$ are aligned, $\theta_{tunnel} = 0°$. Figure 1(c) shows schematics of the first Brillouin zone (BZ) of s-WSe$_2$ and d-WSe$_2$ and momentum-conserved resonant tunneling from s-WSe$_2$ to d-WSe$_2$. When the d-WSe$_2$ flake is twisted with respect to the s-WSe$_2$ flake in real space, the Brillouin zone (BZ) of d-WSe$_2$ is also rotated by θ_{tunnel} around the Γ point relative to that of s-WSe$_2$, as shown in the figure. Hence, for different θ_{tunnel}, the electron tunnels under in-plane momentum conservation from the s-WSe$_2$ Q point into different points in the momentum space of d-WSe$_2$ [red arrow in Fig. 1(c)]; thus the resonant tunneling conditions are dependent on θ_{tunnel}. In contrast, hole resonant tunneling can occur between the Γ points of s-WSe$_2$ and d-WSe$_2$ under any θ_{tunnel} [green arrow in Fig. 1(c)] because the relative Γ point positions between the two WSe$_2$ layers remain unchanged under the control of θ_{tunnel}. Therefore, the twist angle dependence of resonant tunneling is expected to differ between electron and hole tunneling. To confirm this hy-

pothesis, we fabricated devices in which s-WSe$_2$ and d-WSe$_2$ were stacked with $\theta_{tunnel} = 0°$, 15°, 30°, 41°, and 60° [their optical micrographs are shown in Fig. 1(d)] and compared their tunneling transport properties. The source and drain side are defined differently for each measurement (see Appendix D for the measurement circuit). The gate and interlayer bias voltages are applied using a Keithley 2400 Source Measure Unit, and the tunneling current is measured using a current amplifier (DL Instruments, Model 1211). All the measurements are conducted using a variable-temperature cryostat.

First, we show the current density-voltage (J-V_{int}) characteristics of all the devices. The data for electron and hole tunneling are presented in Figs. 1(e) and 1(f), respectively (the detailed gate-voltage dependence of the J-V_{int} curve from each device is presented in Appendix E). For electron tunneling measured at 2 K [Fig. 1(e)], multiple peaks indicated by different symbols (orange circles, blue down-pointing triangles, red up-pointing triangles, and green squares) are observed in the V_{int} range from $V_{int} = 0$ to 1.2 V and they exhibit at different V_{int} positions for different θ_{tunnel} values; thus the result is dependent on θ_{tunnel}. In contrast, the hole tunneling data measured at 300 K [Fig. 1(f)] exhibit multiple peak structures with peak V_{int} positions that are nearly identical for all the devices; thus it is independent of θ_{tunnel}. Therefore, we found that the twist angle dependence of resonant tunneling is remarkably different between the two vdWQW states.
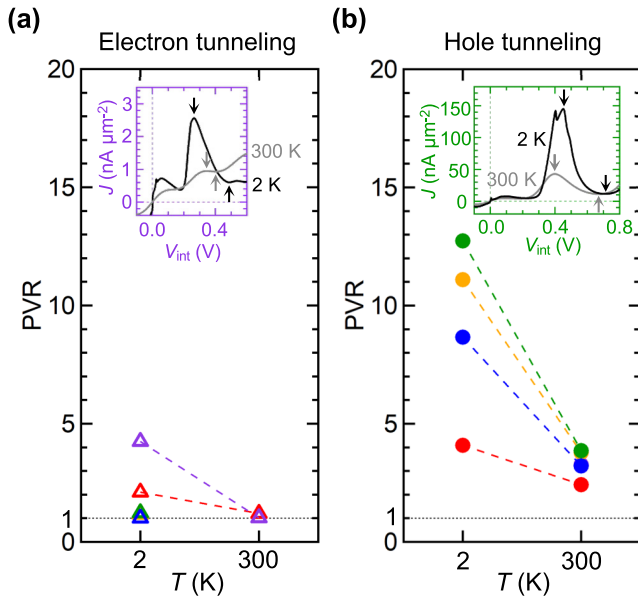
FIG. 4. (a) Peak-to-valley ratio (PVR) obtained from the second peak and valley on the positive V_{int} side in the J-V_{int} data of electron tunneling for each device. The measurement temperatures were 2 and 300 K. Inset: J-V_{int} curves from the $\theta_{tunnel} = 60°$ device at 2 and 300 K under $V_{sg} = 15$ V and $V_{dg} = 60$ V. The positions of the peak and valley currents for calculating the PVRs are indicated by the arrows. (b) PVRs at 2 and 300 K for hole tunneling. Inset: J-V_{int} curves from the $\theta_{tunnel} = 30°$ device at 2 and 300 K under $V_{sg} = -100$ V and $V_{dg} = -12$ V. In these figures, the data for $\theta_{tunnel} = 0°$, 15°, 30°, 41°, and 60° correspond to red, orange, green, blue, and purple marks, respectively.

Next, we discuss the details of the twist angle dependence. First, we focus on the electron tunneling results. The observed peak positions in the J-V_{int} curves of Fig. 1(e) (indicated by different symbols) are plotted with respect to the twist angle θ_{tunnel} in the left panel of Fig. 2(a) [the symbols have the same meaning as those used in Fig. 1(e)]. Overall, the θ_{tunnel} dependence exhibits a period of 60°, showing that V_{int} is greatest near $\theta_{tunnel} = 30°$ and decreases as θ_{tunnel} approaches 0° or 60°. The peak positions for $\theta_{tunnel} = 0°$ are similar to those at 60°. In the figure, the solid lines are the DFT-calculated energies of the vdWQW states of CB along the angular direction of Q-Q'. The experimental result is in good agreement with the calculation, indicating that the θ_{tunnel}-dependent resonant tunneling is dominantly determined by the band dispersion. In the next paragraph, we explain the interpretation for the θ_{tunnel} dependence of the tunneling data.

The influence of θ_{tunnel} on resonant tunneling is twofold. First, θ_{tunnel} changes the momentum-matching condition between s-WSe$_2$ and d-WSe$_2$, as shown in the top row panels of Fig. 2(b). In the figure, the relative orientations of the BZ between s-WSe$_2$ and d-WSe$_2$ are illustrated for different θ_{tunnel}. When $\theta_{tunnel} = 0°$, the Γ-Q-K directions of s-WSe$_2$ and d-WSe$_2$ are aligned in the momentum space. In contrast, when $\theta_{tunnel} > 0°$, the BZ of d-WSe$_2$ rotates around the Γ point relative to that of s-WSe$_2$; therefore, the Γ-Q-K directions of s- and d-WSe$_2$ are no longer aligned. For example, at $\theta_{tunnel} = 30°$, the Γ-Q-K direction of s-WSe$_2$ is aligned with

the Γ-M direction of d-WSe$_2$. Second, θ_{tunnel} changes the matching condition of the band energies of s- and d-WSe$_2$ for the occurrence of resonant tunneling. On the left of the bottom row panel of Fig. 2(b), the CB energy of s-WSe$_2$ along the Γ-Q-K direction is illustrated. For comparison, in the other panels in the bottom row, the CB subbands of d-WSe$_2$ along the direction aligned to the Γ-Q-K direction of s-WSe$_2$ are illustrated for different θ_{tunnel}. Within our experimental range, the Fermi levels (E_F) of both s-WSe$_2$ and d-WSe$_2$ are located close to the bottom of the Q valleys. The position of the bottom of the Q valley is indicated by the momentum k_Q. At $V_{int} = 0$ V, the Fermi levels (E_F) of s- and d-WSe$_2$ are aligned, as indicated by the horizontal dashed line in the figure. As θ_{tunnel} changes from 0° to 60°, the overall band energy of d-WSe$_2$ aligned with the Γ-Q-K direction of s-WSe$_2$ increases toward 30° and then decreases. Owing to the symmetry of 3L WSe$_2$, the energy levels of the band at 60° are the same as those at 0°. Upon applying a positive V_{int} between s- and d-WSe$_2$, the energy of d-WSe$_2$ is lowered with respect to that of s-WSe$_2$. Then, resonant tunneling occurs when the energy of the first subband bottom in s-WSe$_2$ coincides with the energies of the unoccupied subbands of d-WSe$_2$. Hence, for $\theta_{tunnel} = 0°$, the resonant tunneling peaks indicated by the orange circle, blue down-pointing triangle, red up-pointing triangle, and green square can be assigned to resonant tunneling into the first to fourth subbands, respectively, of the d-WSe$_2$ as shown in the figure. Because the subbands are located at higher energies for $\theta_{tunnel} = 15°$, 30°, and 41°, a larger V_{int} is required to observe the resonant tunneling peaks. Therefore, the θ_{tunnel} dependence of electron resonant tunneling tracks the band energies of d-WSe$_2$ along the angular direction of Q-Q' under momentum- and energy-conserved tunneling conditions. More precisely, the intersections between the subbands of d-WSe$_2$ and the vertical dotted line (corresponding to k_Q) provide the resonant tunneling condition. We calculated the angular dispersion at a fixed k_Q using DFT, and plotted it for comparison in Fig. 2(a), which explains the experimental results very well. Therefore, the twist-controlled resonant tunneling based on CB vdWQW is sensitive to the angular dispersion of the band, thus exhibiting periodic modulation on θ_{tunnel} with a period of 60°. Note that while the peak positions of resonant tunneling are similar between the $\theta_{tunnel} = 0°$ and 60° devices, the shapes of their J-V_{int} curves are different; however, its origin is not clear at this point.

It is worth mentioning that both the experiment and calculation show the crossing of the second and third subbands, indicated by the coincidence of red up-pointing triangles and blue down-pointing triangles at $\theta_{tunnel} = 30°$ in Fig. 2(a). Since 3L WSe$_2$ exhibits structural inversion asymmetry, the second and third subbands are spin-polarized bands. The first and fourth bands are spin-degenerate bands. Because the spin direction is opposite between the Q and Q' points, these spin-polarized bands cross along the Γ-M direction. Therefore, three resonant tunneling peaks generated by three spin-degenerate bands should be observed at $\theta_{tunnel} = 30°$, whereas four resonant tunneling peaks, including two spin-polarized bands and two spin-degenerate bands, were observed at θ_{tunnel} values of 0°, 15°, 41°, and 60°.

Next, we discuss the resonant tunneling of the holes. The observed peak positions in the J-V_{int} curves of Fig. 1(f),

marked by purple pentagons and brown left-pointing triangles, are plotted with respect to the twist angle θ_{tunnel} in the left panel of Fig. 2(c), which is nearly independent of θ_{tunnel}. In the case of hole resonant tunneling, it occurs between the VB subbands at the Γ point of s-WSe$_2$ and d-WSe$_2$. Therefore, we plotted the DFT-calculated energy spacing between the first and second VB subbands at the Γ point in the figure as solid lines. The experimentally observed peak positions of resonant tunneling show good agreement with the calculation; thus these peaks can be assigned to hole resonant tunneling from the first subband at the Γ point of s-WSe$_2$ into the first and second subband at the Γ point of d-WSe$_2$ as illustrated in Fig. 2(d). Note the third peak was not observed because it required the application of a larger amplitude of V_{dg} [6], which is limited by the dielectric breakdown of the gate insulator. As can be seen from the figure, the relative positions of the Γ point between s-WSe$_2$ and d-WSe$_2$ remain unchanged with θ_{tunnel}. Therefore, the resonant tunneling should not be significantly dependent on θ_{tunnel} for vdWQW in the VB, as experimentally observed. These results highlight the different twisted-resonant tunneling properties of the vdWQW states in the CB and VB. Moreover, as demonstrated in the CB results, the twisted-resonant tunneling method enables probing of the band dispersion [Fig. 3(a)]. Indeed, these results reveal the unique subband dispersion of the CB-vdWQW states including a saddle point and crossing as shown in Figs. 3(b) and 3(c).

Finally, we discuss the PVR of both electron and hole resonant tunneling, because this value has been used to evaluate the performance of resonant tunneling devices. We collected J-V_{int} data at both 2 and 300 K for electron and hole tunneling, respectively (the J-V_{int} data are presented in Appendix F). The PVRs were calculated for the second resonant tunneling peak on the positive V_{int} side at both 2 and 300 K, and the results are shown in Figs. 4(a) and 4(b). The positions of the peaks and valleys are indicated by the arrows in the insets. At both temperatures, we found that the PVR was significantly larger for hole tunneling than for electron tunneling. Notably, the largest PVR $\sim$12.7, was realized for hole tunneling at 2 K [inset of Fig. 4(b)]. These PVR values are significantly larger than other reported resonant tunneling devices [3,8,10,11,15–17] (see Appendix G, for comparison of PVRs with other devices). In contrast, the PVR is almost unity or not defined due to an absence of the negative differential resistance (NDR) for electron tunneling at 300 K for all θ_{tunnel} [inset of Fig. 4(a)]. These comparisons reveal the advantage of hole tunneling in obtaining a larger PVR. We infer that isotropic dispersion of the VB subbands at the Γ point helps maintain a large overlap between the filled state of s-WSe$_2$ and the unoccupied state of d-WSe$_2$, irrespective of θ_{tunnel}, under momentum- and energy-conserved resonant tunneling. This is difficult to achieve for electron tunneling between the vdWQW states in the CB because any misalignment in θ_{tunnel} reduces the band overlap between the Q point of s-WSe$_2$ and the unoccupied band of d-WSe$_2$ at the resonant tunneling; thus the PVR is decreased. This makes hole resonant tunneling between vd-WQWs in the VB suitable for applications that require a larger PVR.

III. CONCLUSION

In conclusion, we demonstrated 3L-WSe$_2$/h-BN/3L-WSe$_2$ vdW double QW devices by controlling the twist angle θ_{tunnel} between the 3L WSe$_2$ flakes, and investigated the θ_{tunnel} dependence on both electron and hole tunneling behaviors. For electron tunneling, we observed multiple resonant tunneling peaks whose positions were significantly changed with θ_{tunnel} having a periodicity of 60°. However, for hole tunneling, the positions of the resonant tunneling peaks appeared to be independent of θ_{tunnel}. For the PVR of resonant tunneling, we found that hole tunneling exhibits a larger PVR than electron tunneling. These differences between electron and hole tunneling are due to the different position in momentum space and dispersion between CB vdWQW (Q point) and VB vdWQW (Γ point). Our investigations of both the CB- and VB-vdWQW states of FL WSe$_2$ via twist-controlled resonant tunneling provide important clues for the development of the vdWQW technology.

APPENDIX A: DFT CALCULATION OF FEW-LAYER WSe$_2$ SUBBAND ENERGY DISPERSION

We show the band structure of monolayer (1L) to six-layer (6L) WSe$_2$, obtained via DFT calculations, in Fig. 5(a). Details of the calculation method are presented in our previous paper [3]. Subbands appear in both the conduction band (CB) and valence band (VB), as highlighted by the orange and green rectangular outlines. In WSe$_2$ with an even number of layers, the CB subbands at the Q valley are all spin degenerate. In WSe$_2$ with an odd number of layers, the spin degeneracy of one of the subbands at the CB Q valley is lifted due to spatial inversion asymmetry, whereas at this valley, the other subbands are spin degenerate; thus $N + 1$ subbands are observed along Γ-Q-K. However, a different trend is observed for the CB subband structure along Γ-M [Fig. 5(b)]: the number of subbands is found to be equal to N, and all the subbands are spin degenerate. As a result, the CB of three-layer (3L) WSe$_2$ has four subbands along Γ-Q-K and three subbands along Γ-M [Fig. 5(c)]. We show the calculated angular dispersion of 3L WSe$_2$ along Q-Q' in Fig. 5(d). The second- and third-lowest CB subbands at the Q and Q' valleys are spin polarized, and these bands cross at an angle of 30° [corresponding to the Γ-M direction; see Fig. 5(b)].
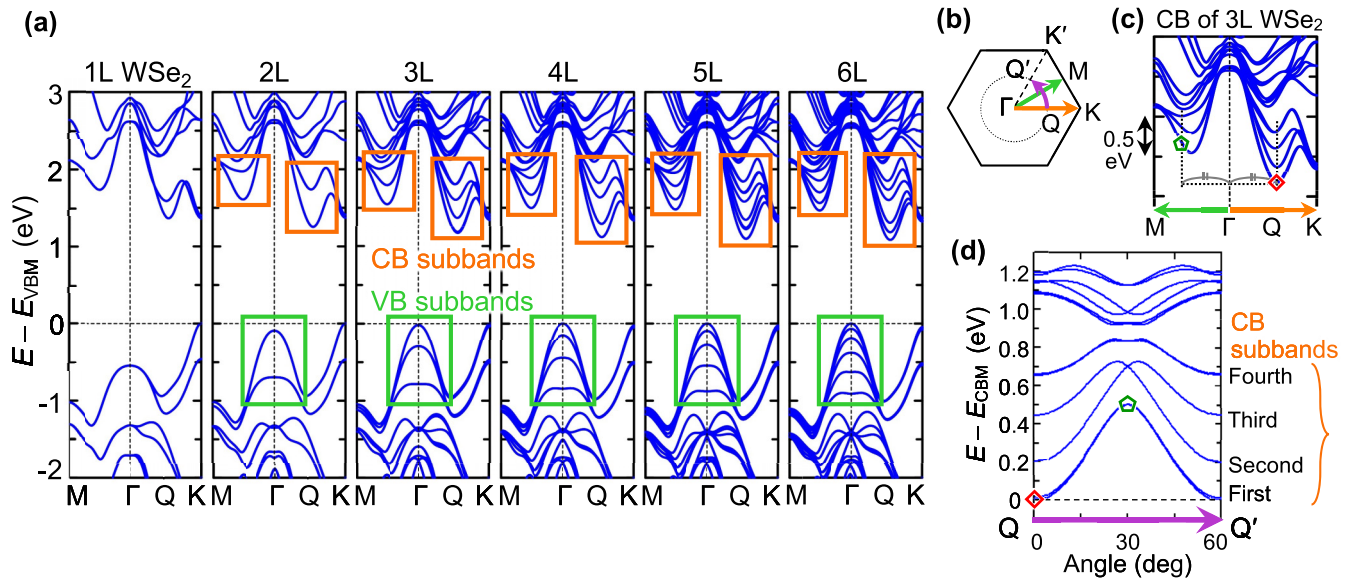
FIG. 5. Band structure of monolayer (1L) to six-layer (6L) WSe_2 obtained via DFT calculations. The subband structures in the conduction band (CB) and valence band (VB) are outlined by orange and green rectangles, respectively. The valence band maximum (VBM) energy is set to 0 eV. (b) Illustration of the first Brillouin zone of WSe_2. (c) Band structure of three-layer (3L) WSe_2 in the CB region. (d) Calculated band energies of 3L WSe_2 plotted along the Q-Q' angular direction. The conduction band minimum (CBM) energy is set to 0 eV. Energies marked by a red diamond and green pentagon correspond to those in (c). The orange, green, and purple arrows indicate the momentum space directions in [(b)–(d)].

APPENDIX B: DEVICE FABRICATION

A WSe_2 bulk crystal was grown via chemical vapor transport (CVT) using iodine as the transport agent. A high-quality bulk crystal of h-BN was grown using high-pressure and high-temperature methods. A natural graphite crystal was purchased from NGS Naturgraphit GmbH. Few-layer (FL) WSe_2 flakes were mechanically exfoliated from the bulk crystal using adhesive tape (SPV-224, Nitto Denko), deposited on a polydimethylsiloxane (PDMS) sheet (PF-40-X4 17MIL, Gel-Pak), and then transferred onto a SiO_2/Si substrate. One-nanometer-thick h-BN and monolayer graphene flakes were mechanically exfoliated from the respective bulk crystals using clean adhesive tape (31 B, Nitto Denko) and directly deposited on a SiO_2/Si substrate. We selected 20- to 50-nm-thick h-BN as the substrate and for encapsulation of the tunnel junction, four- to eight-layer h-BN as the tunnel barrier, 3L WSe_2 as the upper and lower junction layers, and monolayer graphene as the contact layer.

Figure 6(a) shows a schematic of the fabricated device. The center of the structure is the 3L-WSe_2/FL-h-BN/3L-WSe_2 vdW tunnel junction, which is shown in the cross-sectional transmission electron microscope (TEM) image in Fig. 6(b). Various devices were fabricated with the following twist angles θ_{tunnel} between the two 3L WSe_2 flakes: 0°, 15°, 30°, 41°, and 60°. Controlling θ_{tunnel} was achieved via the method illustrated in Fig. 7. First, before stacking the atomic layers, we precut a 3L WSe_2 flake on the substrate using a system composed of an optical microscope and a supercontinuum laser (ROCK-400-4-PP, LEUKOS; pulse width, 6 ps; repetition rate, 60 MHz). Subsequently, the vdW heterostructure was fabricated using a polymer-based pickup method as follows: The top h-BN layer was adhered to poly(bisphenol A

carbonate) (PC) on a PDMS sheet, and using this h-BN, one section of the precut WSe_2 was picked up using the vdW force between h-BN and WSe_2. Then, after picking up the h-BN tunneling barrier, the remaining section of the precut WSe_2 on the substrate was picked up, with the twist angle between the two WSe_2 flakes fixed at a specific value. As shown in Fig. 8, after the tunnel junction had been assembled, the twist angle between the WSe_2 flakes was confirmed as accurate to within ±2° using an optical microscope. Finally, the graphene and bottom h-BN layers were picked up sequentially, and the structure on the PC was transferred onto a 290-nm-thick SiO_2/p-doped Si substrate. The substrate temperature was fixed at 130 °C during the pickup of each flake and then changed to 180 °C to transfer the stack to the substrate.
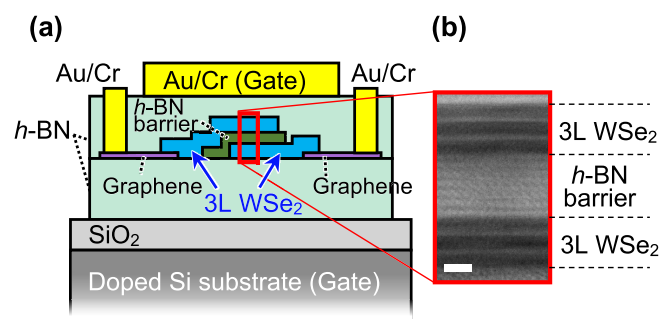

FIG. 6. (a) Schematic of the fabricated devices. The 3L-WSe_2/FL-h-BN/3L-WSe_2 van der Waals (vdW) tunnel junction is encapsulated by top and bottom h-BN layers. (b) Cross-sectional transmission electron microscope (TEM) image of the tunnel junction. The scale bar is 1 nm.
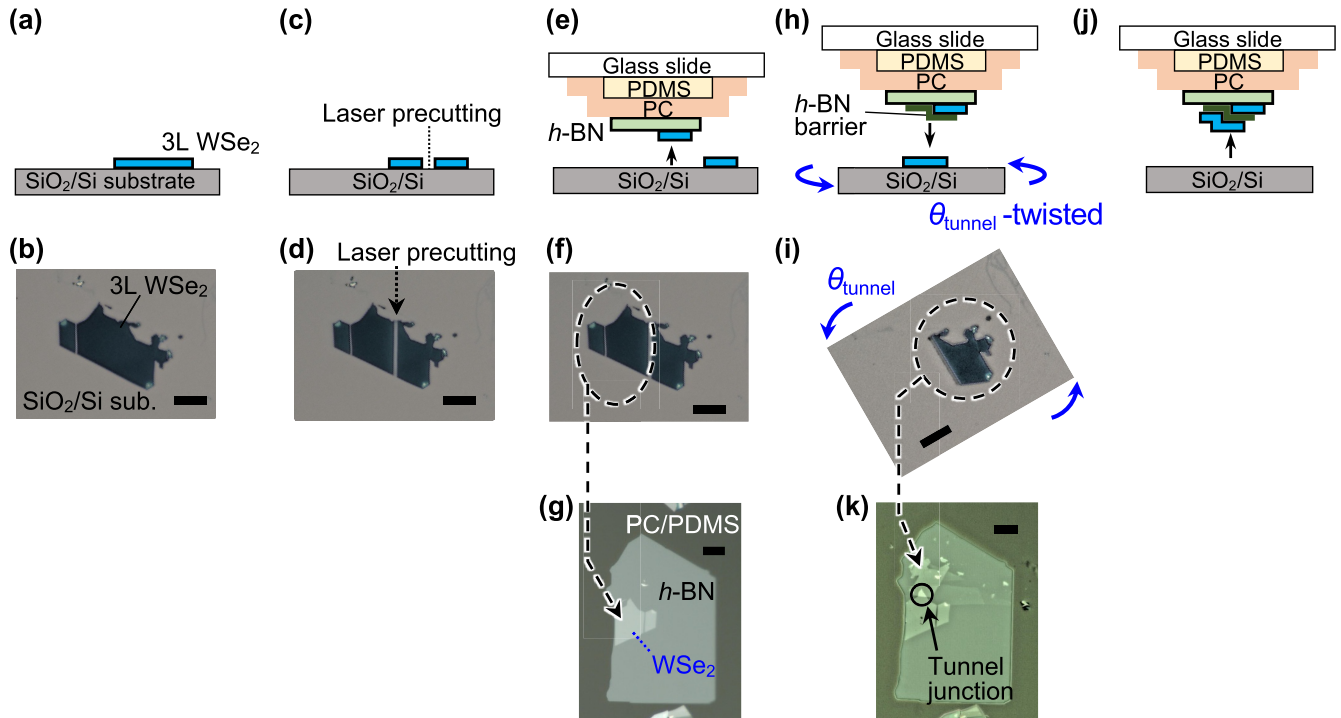
FIG. 7. Schematics [(a), (c), (e), (h), (j)] and optical micrographs [(b), (d), (f), (g), (i), (k)] of the procedure for device construction with control of the twist angle θ_{tunnel} between two 3L WSe$_2$ flakes. [(a), (b)] 3L WSe$_2$ on SiO$_2$ (85 nm)/Si (380 μm) substrate. [(c), (d)] 3L WSe$_2$ after laser precutting. [(e), (f), (g)] Pickup of one section of the WSe$_2$ by the top h-BN layer, which was adhered to a PC/PDMS sheet. [(h), (i)] Rotation of the other section of WSe$_2$ remaining on the substrate and [(j), (k)] its pickup to complete the assembly of the tunnel junction. All scale bars are 10 μm.

Lithography was performed to form electrical contacts with the graphene layers. The structure was spin coated with a poly(methyl methacrylate) (PMMA) resist, and electrode patterns were prepared via electron-beam (EB) lithography. The h-BN and graphene were then exposed to CF$_4$ gas for reactive ion etching (RIE200iP, Samco), and the contact electrodes were deposited by EB evaporation. Au (40–75 nm)/Cr (20 nm, with oblique deposition) was used as

the source and drain electrodes to form ohmic contacts with graphene, and Au (50–75 nm)/Cr (5 nm) was used as the top gate electrode.

APPENDIX C: ELECTRICAL PROPERTY OF GRAPHENE/WSe$_2$ HETEROJUNCTION

Electron and hole contact to 3L WSe$_2$ using graphene contacts is investigated. Figures 9(a) and 9(b) show an optical micrograph and schematic illustration of the device. Under the application of source-drain voltage V_{sd}, current flows between the graphene electrodes through 3L WSe$_2$. The measured characteristics include two of the in-plane transport of graphene, two of the vertical transport at graphene/WSe$_2$ junction, and an in-plane transport of WSe$_2$. During the measurement, top and bottom gate voltages (V_{tg}, V_{bg}) were applied to the Au/Cr electrode and doped Si substrate, respectively; the back gate insulator is 23 nm h-BN/290 nm SiO$_2$, and the top gate insulator is 31 nm h-BN.

We measured the current under sweeping V_{tg} and V_{bg} at fixed V_{sd} of $V_{sd} = 0.3$ V. Figures 9(c) and 9(d) show V_{tg} sweep ranging from -6 to 10 V at different values of V_{bg} measured at $T = 300$ and 2 K, respectively. Similarly, Figs. 9(e) and 9(f) show the V_{bg} sweep ranging from -70 to 70 V at different values of V_{tg}. By using graphene electrodes, we achieved the detection of both electron and hole currents. Both of the currents were significantly magnified under simultaneous application of large positive or negative gate voltages of V_{tg} and V_{bg}.
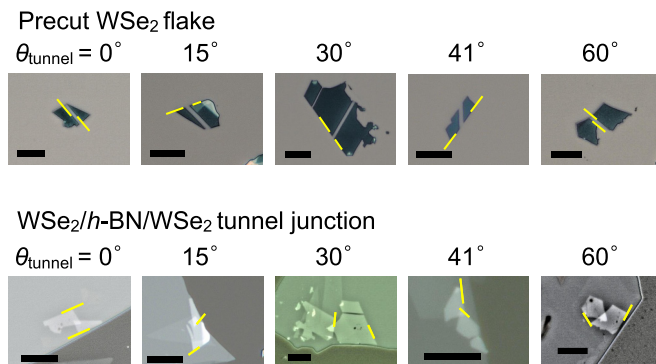

FIG. 8. Upper images: optical micrographs of precut WSe$_2$ flakes on SiO$_2$/Si substrate. Lower images: optical micrographs of fabricated tunnel junctions on PC/PDMS. All scale bars are 10 μm. Yellow lines highlight pairs of representative edges of the WSe$_2$ flakes that are parallel in each of upper panels. After fabricating the tunnel junction (lower panels), the angle between the yellow lines in each image is set to the chosen value for the device.
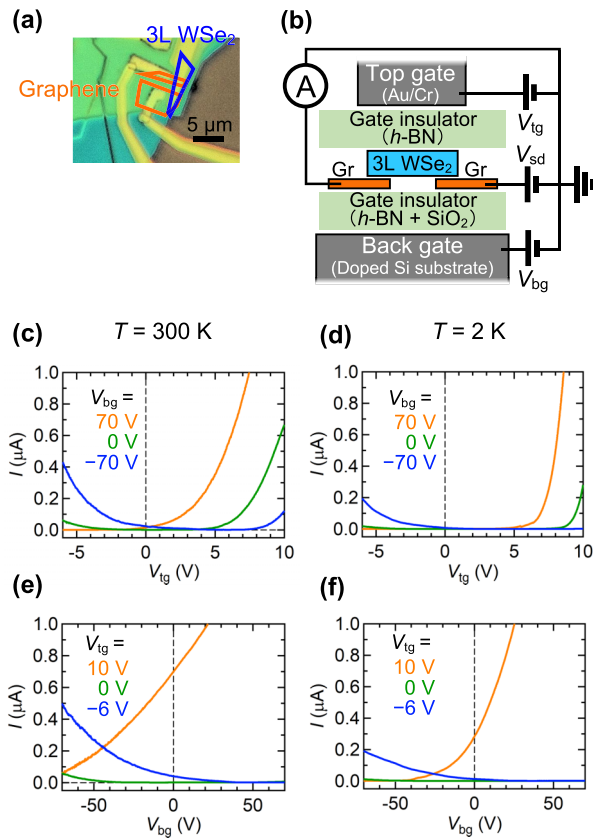
FIG. 9. (a) Optical micrograph of the measured device. (b) Schematics of the measurement circuit. [(c), (d)] I-V_{tg} characteristics under different values of V_{bg} measured at (c) 300 K and (d) 2 K. [(e), (f)] I-V_{bg} characteristics under different values of V_{tg} measured at (e) 300 K and (f) 2 K. V_{sd} is fixed at 0.3 V in [(c)–(f)].
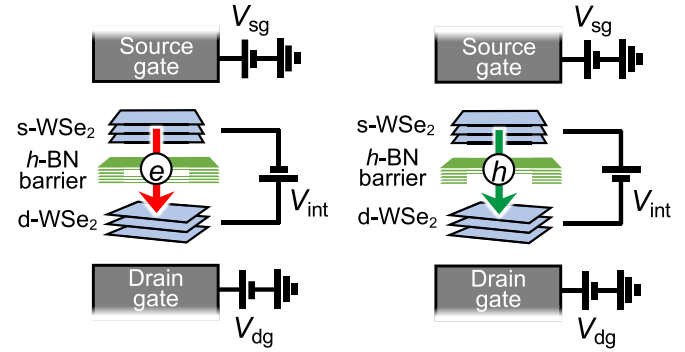

FIG. 11. Schematic of the measurement circuit for (left) electron tunneling and (right) hole tunneling. Source and drain gate voltages (V_{sg} and V_{dg}) are applied to control carrier densities in the source WSe$_2$ (s-WSe$_2$) and drain WSe$_2$ (d-WSe$_2$), respectively.

APPENDIX D: MEASUREMENT CIRCUIT

Figure 10 shows a measurement circuit of electron tunneling (ET) and hole tunneling (HT) for each device. We conducted four-terminal measurement for the $\theta_{tunnel} = 0°$ device and two-terminal measurement for the other devices. In the $\theta_{tunnel} = 0°$ device, the source WSe$_2$ (s-WSe$_2$) and drain WSe$_2$ (d-WSe$_2$) each had two graphene contacts. One contact for each WSe$_2$ flake was used for the electric circuit, in which an interlayer bias was applied, and the tunneling current was measured. The other contact in each WSe$_2$ flake was used to measure the interlayer potential difference, V_{int}. For the other devices, only one contact for each WSe$_2$ flake was used to apply an interlayer bias, V_{int}, while the tunneling current was measured.

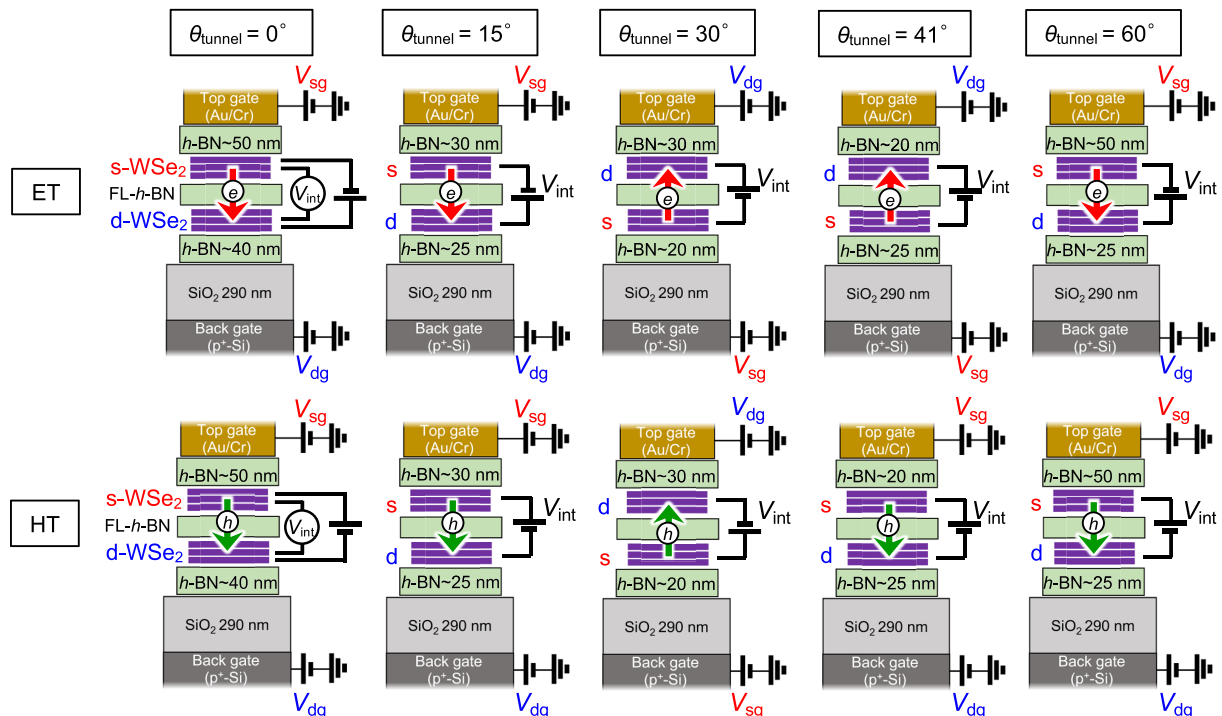FIG. 10. Measurement circuit of electron tunneling (ET) and hole tunneling (HT) for each device.
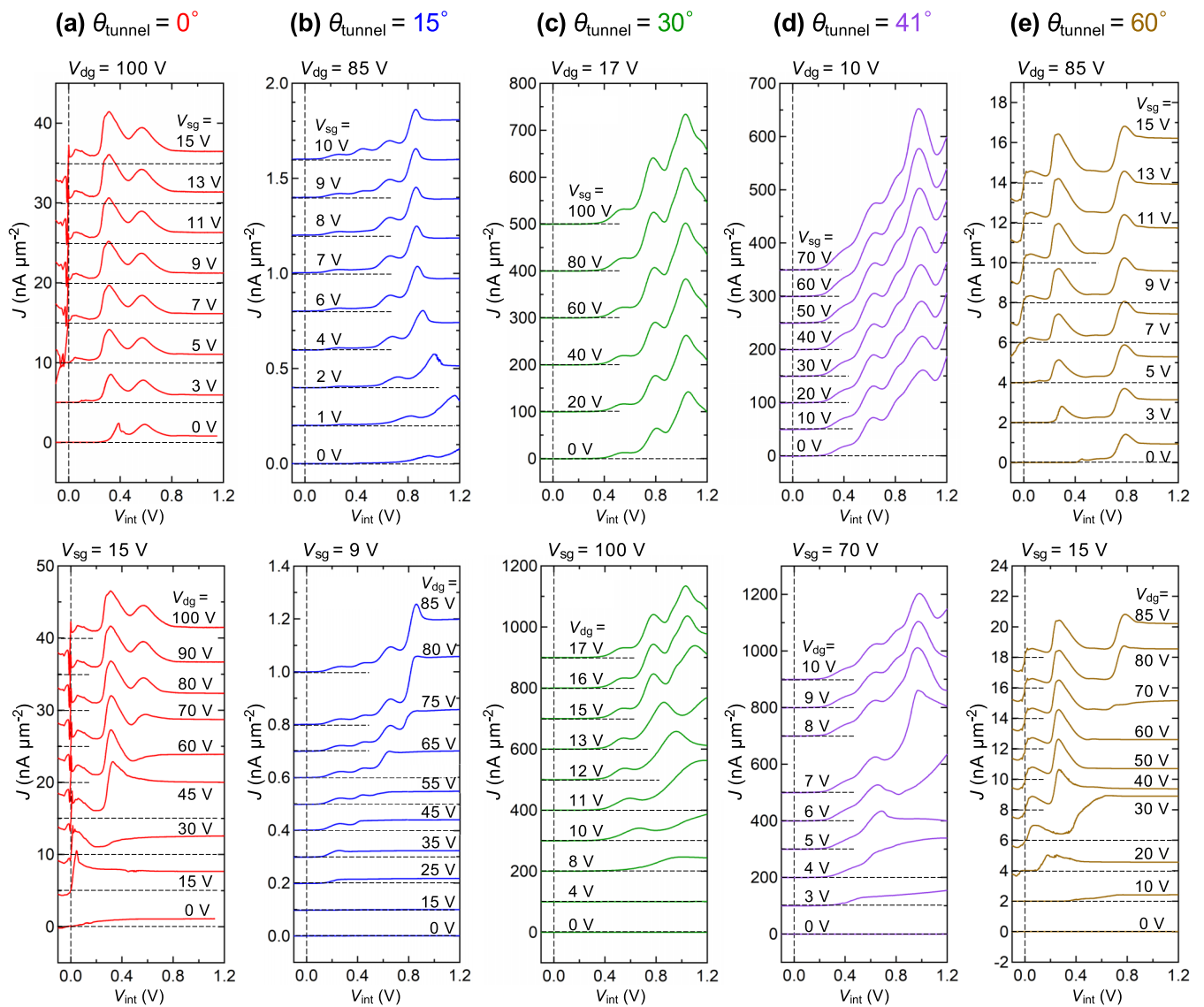
Electron tunneling

FIG. 12. [(a)–(e)] J-V_{int} characteristics for electron tunneling measured at 2 K from the devices having θ_{tunnel} values of (a) 0°, (b) 15°, (c) 30°, (d) 41°, and (e) 60°. Each panel includes results measured at different V_{sg} with fixed V_{dg} (upper panels) and at different V_{dg} with fixed V_{sg} (lower panels). Traces are offset for clarity, and $J = 0$ is indicated for each trace by a horizontal dashed line.

APPENDIX E: GATE-VOLTAGE DEPENDENCE OF THE J-V_{int} CURVE FROM EACH DEVICE

We measured the gate-voltage dependence of the J-V_{int} curve from each device. Figure 11 illustrates the device structure. By changing positive source and drain gate voltages V_{sg} and V_{dg}, electron densities in s-WSe$_2$ and d-WSe$_2$, respectively, can be tuned. Similarly, negative V_{sg} and V_{dg} can alter hole densities in s-WSe$_2$ and d-WSe$_2$. The results for the electron and hole tunneling are presented in Figs. 12 and 13, respectively. The influence of V_{sg} and V_{dg} on the J-V_{int} curve is different owing to the interlayer bias V_{int} [6]. Upon enhancing the amplitudes of these gate voltages from

0 V, carriers were accumulated in WSe$_2$ within the tunnel junction region. Then the peak structures in the J-V_{int} curves became obvious. Meanwhile, the series resistance, including the in-plane WSe$_2$ channel and graphene/WSe$_2$ heterojunction, decreased. When the gate voltages were sufficiently high, the series resistance was negligibly small compared with the resistance of the tunnel junction; thus the entirety of V_{int} was applied to the tunnel junction. Consequently, the V_{int} positions of the observable peaks were found to be independent of the gate voltage in the high-voltage region.
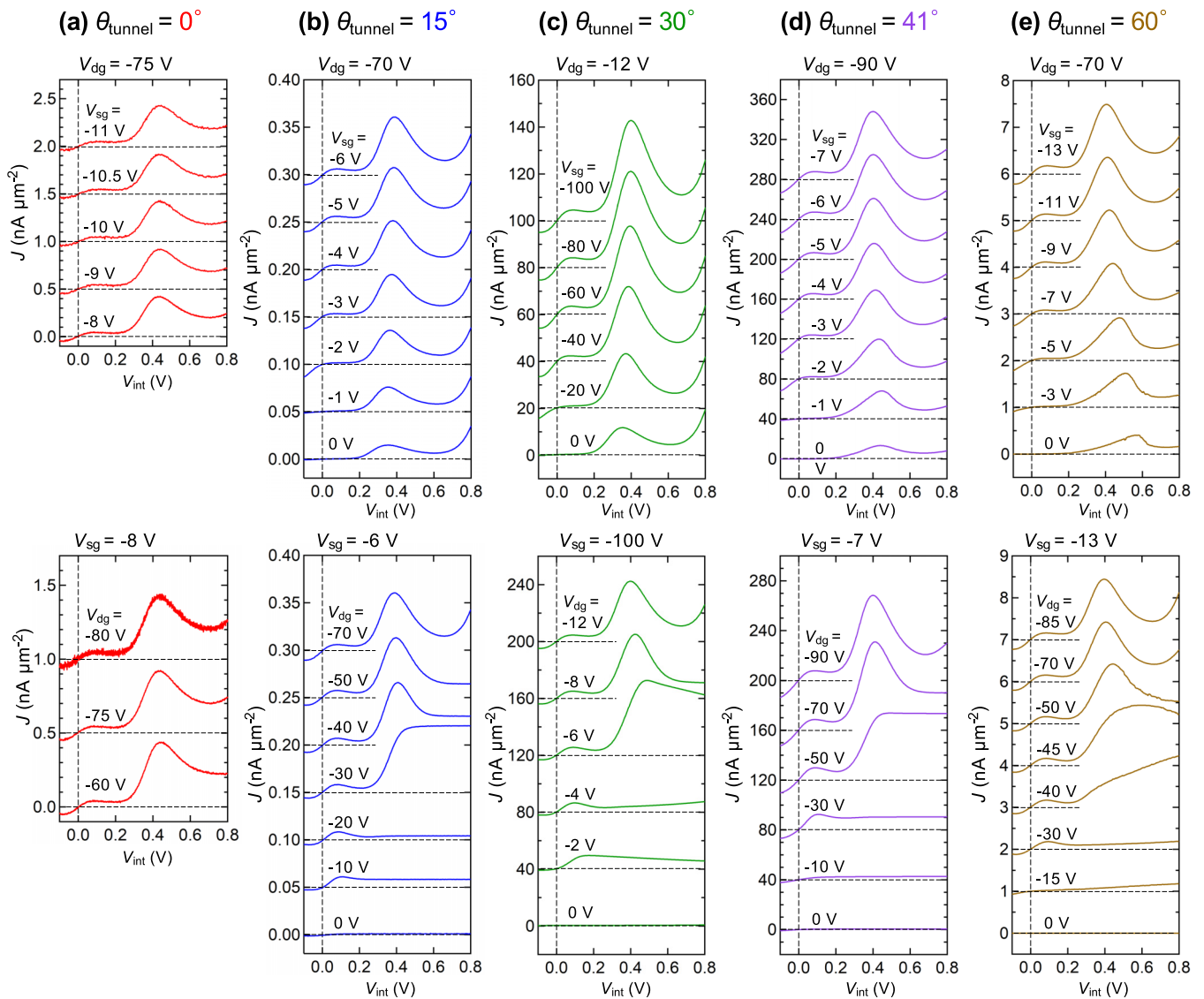
FIG. 13. [(a)–(e)] J-V_{int} characteristics for hole tunneling measured at 300 K from the devices having θ_{tunnel} values of (a) 0°, (b) 15°, (c) 30°, (d) 41°, and (e) 60°. Each panel includes results measured at different V_{sg} with fixed V_{dg} (upper panels) and at different V_{dg} with fixed V_{sg} (lower panels). Traces are offset for clarity, and $J = 0$ is indicated for each trace by a horizontal dashed line.

APPENDIX F: GATE-VOLTAGE DEPENDENCE OF THE J-V_{int} CURVE FROM EACH DEVICE

Figure 14 shows J-V_{int} characteristics measured at 2 and 300 K. From these data, PVRs are calculated by current values of the peak and valley (their positions are indicated by arrows in the figure), and compared in Fig. 4 of the main text.

APPENDIX G: COMPARISON OF PVRs WITH OTHER REPORTED RESONANT TUNNELING DEVICES

We compare the PVR values obtained in this study with those reported in the literature, as shown in Fig. 15. For resonant tunneling of holes between the VB Γ points, the PVR values are larger than those reported in the literature [3,8,10,11,15–17].
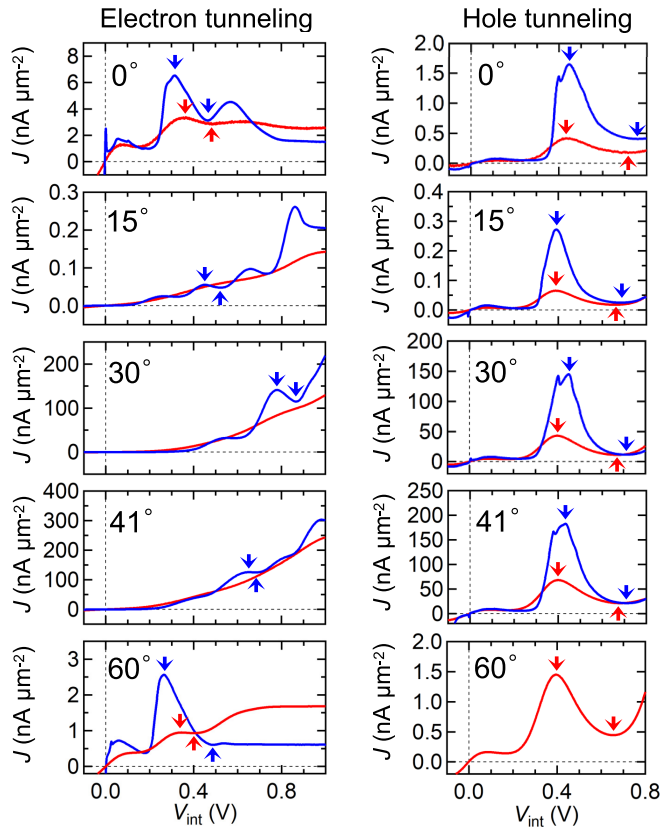
FIG. 14. J-V_{int} characteristics measured at 2 K (blue) and 300 K (red). Positions of the peak and valley used for calculating PVRs in the main text are indicated by arrows. Gate-voltage conditions for electron tunneling: $V_{sg} = 15$ V, $V_{dg} = 100$ V for 0°; $V_{sg} = 10$ V, $V_{dg} = 85$ V for 15°; $V_{sg} = 100$ V, $V_{dg} = 17$ V for 30°; $V_{sg} = 70$ V, $V_{dg} = 10$ V for 41°; and $V_{sg} = 15$ V, $V_{dg} = 60$ V for 60°. Gate-voltage conditions for hole tunneling: $V_{sg} = -10.5$ V, $V_{dg} = -75$ V for 0°; $V_{sg} = -6$ V, $V_{dg} = -70$ V for 15°; $V_{sg} = -100$ V, $V_{dg} = -12$ V for 30°; $V_{sg} = -7$ V, $V_{dg} = -90$ V for 41°; and $V_{sg} = -13$ V, $V_{dg} = -85$ V for 60°.
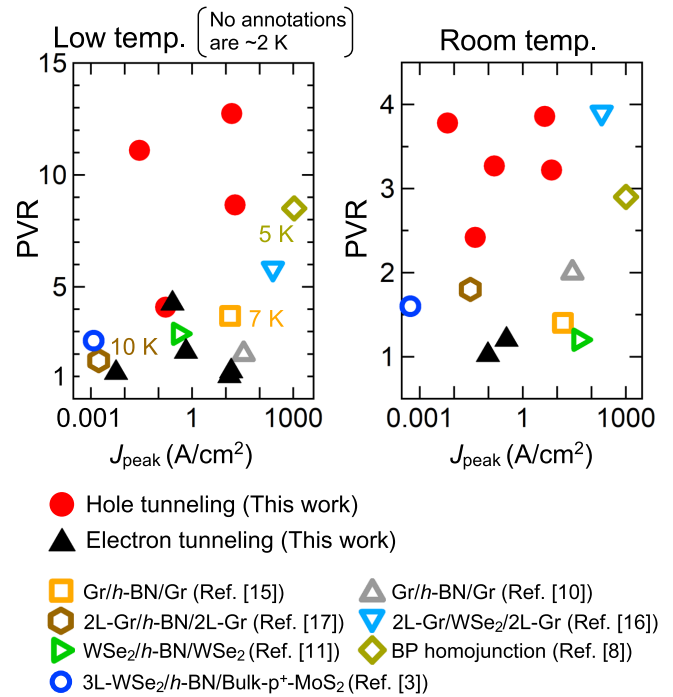
FIG. 15. Peak-to-valley ratio (PVR) plotted against peak current density at low temperature (left) and room temperature (right).

[1] D. A. Ruiz-Tijerina, M. Danovich, C. Yelgel, V. Zólyomi, and V. I. Fal'ko, Hybrid **k·p** tight-binding model for subbands and infrared intersubband optics in few-layer films of transition-metal dichalcogenides: MoS$_2$, MoSe$_2$, WS, and WSe$_2$, Phys. Rev. B **98**, 035411 (2018).

[2] P. Schmidt, F. Vialla, S. Latini, M. Massicotte, K.-J. Tielrooij, S. Mastel, G. Navickaite, M. Danovich, D. A. Ruiz-Tijerina, C. Yelgel, V. Fal'ko, K. S. Thygesen, R. Hillenbrand, and F. H. L. Koppens, Nano-imaging of intersubband transitions in van der Waals quantum wells, Nat. Nanotechnol. **13**, 1035 (2018).

[3] K. Takeyama, R. Moriya, S. Okazaki, Y. Zhang, S. Masubuchi, K. Watanabe, T. Taniguchi, T. Sasagawa, and T. Machida, Resonant tunneling due to van der Waals quantum-well states of few-layer WSe$_2$ in WSe$_2$/h−BN/p^+−MoS$_2$ junction, Nano Lett. **21**, 3929 (2021).

[4] H.-Y. Deng, Near-infrared quantum cascade lasers designed with van der Waals materials, Phys. Rev. Appl. **16**, 044038 (2021).

[5] N. Liu, M. Dan, G. Hu, and Y. Zhang, Piezo-phototronic intersubband terahertz devices based on layer-dependent van der Waals quantum well, Nano Energy **94**, 106912 (2022).

[6] K. Kinoshita, R. Moriya, S. Okazaki, Y. Zhang, S. Masubuchi, K. Watanabe, T. Taniguchi, T. Sasagawa, and T. Machida, Resonant tunneling between quantized subbands in van der Waals double quantum well structure based on few-layer WSe$_2$, Nano Lett. **22**, 4640 (2022).

[7] J. Zultak, S. J. Magorrian, M. Koperski, A. Garner, M. J. Hamer, E. Tóvári, K. S. Novoselov, A. A. Zhukov, Y. Zou, N. R. Wilson, S. J. Haigh, A. V. Kretinin, V. I. Fal'ko, and R. Gorbachev, Ultra-thin van der Waals crystals as semiconductor quantum wells, Nat. Commun. **11**, 125 (2020).

[8] P. K. Srivastava, Y. Hassan, D. J. P. de Sousa, Y. Gebredingle, M. Joe, F. Ali, Y. Zheng, W. J. Yoo, S. Ghosh, J. T. Teherani, B. Singh, T. Low, and C. Lee, Resonant tunnelling diodes based on twisted black phosphorus homostructures, Nat. Electron. **4**, 269 (2021).

[9] Z. R. Kudrynskyi, J. Kerfoot, D. Mazumder, M. T. Greenaway, E. E. Vdovin, O. Makarovsky, Z. D. Kovalyuk, L. Eaves, P. H. Beton, and A. Patanè, Resonant tunnelling into the two-dimensional subbands of InSe layers, Commun. Phys. **3**, 16 (2020).

[10] A. Mishchenko, J. S. Tu, Y. Cao, R. V. Gorbachev, J. R. Wallbank, M. T. Greenaway, V. E. Morozov, S. V. Morozov, M. J. Zhu, S. L. Wong, F. Withers, C. R. Woods, Y. J. Kim, K. Watanabe, T. Taniguchi, E. E. Vdovin, O. Makarovsky, T. M. Fromhold, V. I. Fal'ko, A. K. Geim *et al.*, Twist-controlled resonant tunnelling in graphene/boron nitride/graphene heterostructures, Nat. Nanotechnol. **9**, 808 (2014).

[11] K. Kim, N. Prasad, H. C. P. Movva, G. W. Burg, Y. Wang, S. Larentis, T. Taniguchi, K. Watanabe, L. F. Register, and E. Tutuc, Spin-conserving resonant tunneling in twist-controlled WSe$_2$-hBN-WSe$_2$ heterostructures, Nano Lett. **18**, 5967 (2018).

[12] A. Inbar, J. Birkbeck, J. Xiao, T. Taniguchi, K. Watanabe, B. Yan, Y. Oreg, A. Stern, E. Berg, and S. Ilani, The quantum twisting microscope, Nature (London) **614**, 682 (2023).

[13] K. Kim, M. Yankowitz, B. Fallahazad, S. Kang, H. C. P. Movva, S. Huang, S. Larentis, C. M. Corbet, T. Taniguchi, K. Watanabe, S. K. Banerjee, B. J. LeRoy, and E. Tutuc, van der Waals heterostructures with high accuracy rotational alignment, Nano Lett. **16**, 1989 (2016).

[14] P. K. Poddar, Y. Zhong, A. J. Mannix, F. Mujid, J. Yu, C. Liang, J.-H. Kang, M. Lee, S. Xie, and J. Park, Resist-free lithography for monolayer transition metal dichalcogenides, Nano Lett. **22**, 726 (2022).

[15] L. Britnell, R. V. Gorbachev, A. K. Geim, L. A. Ponomarenko, A. Mishchenko, M. T. Greenaway, T. M. Fromhold, K. S. Novoselov, and L. Eaves, Resonant tunnelling and negative differential conductance in graphene transistors, Nat. Commun. **4**, 1794 (2013).

[16] G. W. Burg, N. Prasad, B. Fallahazad, A. Valsaraj, K. Kim, T. Taniguchi, K. Watanabe, Q. Wang, M. J. Kim, L. F. Register, and E. Tutuc, Coherent interlayer tunneling and negative differential resistance with high current density in double bilayer graphene–WSe$_2$ heterostructures, Nano Lett. **17**, 3919 (2017).

[17] B. Fallahazad, K. Lee, S. Kang, J. Xue, S. Larentis, C. Corbet, K. Kim, H. C. P. Movva, T. Taniguchi, K. Watanabe, L. F. Register, S. K. Banerjee, and E. Tutuc, Gate-tunable resonant tunneling in double bilayer graphene heterostructures, Nano Lett. **15**, 428 (2015).